Novel strategy for low-temperature, high-rate growth of dense, hard, and stress-free refractory ceramic thin films

Grzegorz Greczynski, Jun Lu, Stephan Bolz, Werner Koelker, Christoph Schiffers, Oliver Lemmer, Ivan Petrov, Joseph E Greene and Lars Hultman

Linköping University Post Print

N.B.: When citing this work, cite the original article.

Novel strategy for low-temperature, high-rate growth of dense, hard, and stress-free refractory ceramic thin films

Grzegorz Greczynski, Jun Lu, Stephan Bolz, Werner Kölker, Christoph Schiffers, Oliver Lemmer, Ivan Petrov, Joseph E. Greene, and Lars Hultman

Articles you may be interested in
Mechanical behavior of mesoporous titania thin films
Appl. Phys. Lett. **104**, 241902 (2014); 10.1063/1.4883260

Toughness enhancement in hard ceramic thin films by alloy design
APL Mat. **1**, 042104 (2013); 10.1063/1.4822440

Nanomechanical properties of sputter-deposited HfO2 and HfxSi1-xO2 thin films
J. Appl. Phys. **110**, 043527 (2011); 10.1063/1.3627155

Modulation periodicity dependent structure, stress, and hardness in NbN/W2N nanostructured multilayer films
J. Appl. Phys. **109**, 123525 (2011); 10.1063/1.3598083

X-ray diffraction study of stress relaxation in cubic boron nitride films grown with simultaneous medium-energy ion bombardment
Appl. Phys. Lett. **85**, 5905 (2004); 10.1063/1.1836868

Novel strategy for low-temperature, high-rate growth of dense, hard, and stress-free refractory ceramic thin films

Grzegorz Greczynski[a)] and Jun Lu
Department of Physics (IFM), Linköping University, SE-581 83 Linköping, Sweden

Stephan Bolz, Werner Kölker, Christoph Schiffers, and Oliver Lemmer
CemeCon AG, Adenauerstr. 20 A4, D-52146 Würselen, Germany

Ivan Petrov and Joseph E. Greene
Department of Physics (IFM), Linköping University, SE-581 83 Linköping, Sweden and Department of Materials Science, Physics, and the Frederick Seitz Materials Research Laboratory, University of Illinois, Urbana, Illinois 61801

Lars Hultman
Department of Physics (IFM), Linköping University, SE-581 83 Linköping, Sweden

Growth of fully dense refractory thin films by means of physical vapor deposition (PVD) requires elevated temperatures T_s to ensure sufficient adatom mobilities. Films grown with no external heating are underdense, as demonstrated by the open voids visible in cross-sectional transmission electron microscopy images and by x-ray reflectivity results; thus, the layers exhibit low nanoindentation hardness and elastic modulus values. Ion bombardment of the growing film surface is often used to enhance densification; however, the required ion energies typically extract a steep price in the form of residual rare-gas-ion-induced compressive stress. Here, the authors propose a PVD strategy for the growth of dense, hard, and stress-free refractory thin films at low temperatures; that is, with no external heating. The authors use TiN as a model ceramic materials system and employ hybrid high-power pulsed and dc magnetron co-sputtering (HIPIMS and DCMS) in Ar/N_2 mixtures to grow dilute $Ti_{1-x}Ta_xN$ alloys on Si(001) substrates. The Ta target driven by HIPIMS serves as a pulsed source of energetic Ta^+/Ta^{2+} metal–ions, characterized by *in-situ* mass and energy spectroscopy, while the Ti target operates in DCMS mode (Ta-HIPIMS/Ti-DCMS) providing a continuous flux of metal atoms to sustain a high deposition rate. Substrate bias V_s is applied in synchronous with the Ta-ion portion of each HIPIMS pulse in order to provide film densification by heavy-ion irradiation ($m_{Ta} = 180.95$ amu versus $m_{Ti} = 47.88$ amu) while minimizing Ar^+ bombardment and subsequent trapping in interstitial sites. Since Ta is a film constituent, primarily residing on cation sublattice sites, film stress remains low. Dense $Ti_{0.92}Ta_{0.08}N$ alloy films, 1.8 μm thick, grown with $T_s \leq 120\,^\circ$C (due to plasma heating) and synchronized bias, $V_s = 160$ V, exhibit nanoindentation hardness $H = 25.9$ GPa and elastic modulus $E = 497$ GPa compared to 13.8 and 318 GPa for underdense Ti-HIPIMS/Ti-DCMS TiN reference layers ($T_s < 120\,^\circ$C) grown with the same V_s, and 7.8 and 248 GPa for DCMS TiN films grown with no applied bias ($T_s < 120\,^\circ$C). $Ti_{0.92}Ta_{0.08}N$ residual stress is low, $\sigma = -0.7$ GPa, and essentially equal to that of Ti-HIPIMS/Ti-DCMS TiN films grown with the same substrate bias. © *2014 American Vacuum Society*. [http://dx.doi.org/10.1116/1.4884575]

I. INTRODUCTION

The quest for low-temperature processes for the growth of dense, hard, low-stress refractory thin films has been a recurring theme in materials science for many decades.[1–10] The use of inert-gas ion irradiation,[1,2,7] to provide dynamic ion mixing and ion-bombardment-enhanced surface adatom mobilities[3,7,11] during physical vapor deposition, is widely employed for improving film density. However, progress achieved in low temperature densification often comes at the price of incorporating large compressive stresses due to trapping of inert gas ions, and recoil implantation of surface atoms, into film interstitial sites.[3,11–18]

Here, we demonstrate a new strategy for synthesizing high-hardness, low-stress ceramic thin films at low growth temperatures ($T_s \leq 120\,^\circ$C) based upon reactive hybrid high-power pulsed and dc magnetron co-sputtering (HIPIMS/DCMS) with synchronized substrate bias[19–21] with synchronized substrate bias in which a small concentration of a high-mass metal element, with a low first-ionization potential IP_1, is provided during HIPIMS pulses. As an example of this approach, we deposit cubic NaCl-structure TiN by high-rate DCMS from a Ti (47.88 amu) target and add TaN to form a dilute solid solution (TiN and TaN exhibit complete solid solubility)[22] using HIPIMS/DCMS co-sputtering from a Ta (180.95 amu) target in mixed Ar/N_2 discharges. A negative substrate bias V_s is applied in synchronous with the metal–ion portion (2% duty cycle) of each HIPIMS pulse. The growing film is at floating potential, $V_f = 10$ V, between HIPIMS pulses. The

a)Electronic mail: grzgr@ifm.liu.se

relatively low first and second ionization potentials of Ta ($IP_1 = 7.91$ and $IP_2 = 15.60$ eV)[23,24] compared with those of Ar ($IP_1 = 15.76$ eV and $IP_2 = 27.63$ eV),[25] the principal discharge gas, provides significant Ta^+ ion fluxes to the growth surface, as determined by *in-situ* mass spectroscopy, resulting in film densification by generating large numbers of low-energy N and Ti primary recoils with significant cascade overlap leading to efficient ion-irradiation-induced mixing.

Film microstructure evolves from underdense with both intra- and intercolumnar porosity, as determined by cross-sectional transmission electron microscopy (XTEM), scanning electron microscopy (XSEM), and x-ray reflectivity (XRR) results for TiN and $Ti_{0.92}Ta_{0.08}N$ reference layers deposited at low T_s with no Ta ion irradiation, to essentially fully dense for Ta-HIPIMS/Ti-DCMS $Ti_{0.92}Ta_{0.08}N$ polycrystalline layers grown at low T_s with synchronized $V_s = 160$ V Ta ion irradiation. In addition, the hardness and elastic modulus of Ta-HIPIMS/Ti-DCMS $Ti_{0.92}Ta_{0.08}N$ alloys increase with increasing substrate bias from 14.4 and 346 GPa with $V_s = 20$ V to 25.9 and 497 GPa with $V_s = 160$ V. Since Ta ions are film constituents, layer stress remains low ($\sigma \leq -0.7$ GPa). Moreover, due to the low substrate-bias duty cycle, heating generated by pulsed Ta^{n+} ion bombardment is negligible. The deposition rate is maintained high by continuous DCMS sputtering of the Ti target. Further increases in $V_s > 160$ V have no significant effect on H and E, but film compressive stress increases.

II. EXPERIMENT

$Ti_{1-x}Ta_xN$ films are grown in a CC800/9 CemeCon AG magnetron sputtering system[26] equipped with cast rectangular 8.8×50 cm^2 Ti and Ta targets. Si(001) substrates, 2×1 cm^2, are mounted symmetrically with respect to the targets, which are tilted toward the substrate, resulting in a 21° angle between the substrate normal and the normal to each target. Target-to-substrate distance is 18 cm, and the system base pressure is 3.8×10^{-7} Torr (0.05 mPa). The substrates are cleaned sequentially in acetone and isopropyl alcohol and mounted with clips such that their long sides are parallel to the long sides of the targets. The growth chamber is degassed before deposition by applying 0.5 kW to each of two resistive heaters for 1 h, resulting in a chamber temperature of 110 °C at the substrate position; the power is then switched off 1 h prior to the start of film growth such that the substrate temperature T_s drops to 65 °C. T_s is monitored during the deposition process with a calibrated[27] thermocouple attached to a sacrificial dummy substrate. The Ar flow rate is set at 350 cm^3/min, while the N_2 flow is controlled by an automatic pressure regulator via a feedback loop to maintain the total pressure P_{tot} constant during deposition at 3 mTorr (0.4 Pa).

A hybrid target power scheme is employed in which the Ta magnetron is operated in HIPIMS mode to supply a pulsed Ta-ion flux, while the Ti target is operated as a conventional dc magnetron (Ta-HIPIMS/Ti-DCMS).[19] The Ta^+ and Ta^{2+} metal–ion fluxes incident at the film growth surface, and hence, the TaN concentration in $Ti_{1-x}Ta_xN$ films,

is controlled by varying the average power to the HIPIMS target from 0.5 to 1.5 kW, at a fixed pulsing frequency of 100 Hz (2% duty cycle). This corresponds to varying the pulse energy E_p from 5 to 15 J. The peak target current density J_T during the HIPIMS pulse is 0.21 A/cm^2 with $E_p = 5$ J, and increases to 0.53 and 0.93 A/cm^2 with E_p values of 10 and 15 J.[28] Resulting TaN concentrations range from $x = 0.08$ ($E_p = 5$ J) to 0.16 ($E_p = 15$ J) as determined by energy-dispersive x-ray spectroscopy (EDS). The power to the dc magnetron is maintained constant at 6 kW corresponding to a TiN deposition rate of 277 Å/min. Deposition rates for Ta-HIPIMS/Ti-DCMS $Ti_{0.92}Ta_{0.08}N$ films range from 340 Å/min with $V_s = 20$ V to 295 Å/min with $V_s = 280$ V.

A pulsed substrate bias V_s is synchronized with the 200 μs metal–ion-rich portion of each HIPIMS pulse beginning at $t_{offset} = 80$ μs after pulse initiation ($t = 0$ μs), as determined by time-resolved ion mass spectroscopy analyses at the substrate position. At all other times, the substrate is at a negative floating potential $V_s = V_f = 10$ V. For films grown with $E_p = 5$ J, V_s is varied from 20 to 280 V in order to probe the effects of incident Ta ion energy on film nanostructure. The total film deposition time is 60 min, and the resulting film thicknesses range from 2.04 μm at $V_s = 20$ V to 1.77 μm with $V_s = 280$ V. In addition, $Ti_{1-x}Ta_xN$ layers grown with $E_p = 10$ J and V_s varied from 20 to 80 V, as well as with $E_p = 15$ J and V_s varied from 20 to 60 V, are synthesized to investigate the effect of higher Ta^+/Ta^{2+} metal–ion fluxes on film properties.

TiN/$Ti_{0.92}Ta_{0.08}N$/TiN trilayer stacks with total thicknesses of ∼3 μm are used for comparative XTEM nanostructural analyses. The DCMS TiN under- and overlayers are grown with $V_s = 10$ V, and a metal–ion-synchronized substrate bias of $V_s = 160$ V is applied during growth of the $Ti_{0.92}Ta_{0.08}N$ intermediate layer.

Pure DCMS TiN and $Ti_{0.92}Ta_{0.08}N$ reference films are deposited by conventional dc magnetron sputtering at an average power of 6 kW and a floating potential $V_s = 10$ V with no intentional heating ($T_s < 120$ °C). In addition, a DCMS TiN reference film is grown with continuous applied bias $V_s = 60$ V at $T_s = 500$ °C. Ti-HIPIMS/Ti-DCMS TiN reference layers are also grown, following the same procedure as for the Ta-HIPIMS/Ti-DCMS layers (pulsing frequency of 100 Hz, 2% duty cycle, $E_p = 5$ J, and $J_T = 0.30$ A/cm^2), except that the growing films are subjected to Ti^+/Ti^{2+}, rather than Ta^+/Ta^{2+}, irradiation initiated at $t_{offset} = 40$ μs during the synchronously biased metal–ion portion of each HIPIMS pulse.

Time-dependent *in-situ* mass and energy spectroscopy analyses of the ion fluxes incident at the substrate for Ta and Ti targets operated in HIPIMS mode are carried out using a Hiden Analytical EQP1000 instrument to determine the composition, charge state, and energy of ion fluxes incident at the growing film as a function of E_p. In these experiments, the orifice of the mass spectrometer is placed parallel to the target surface at the substrate position. Ion-energy-distribution functions (IEDFs) are recorded in HIPIMS mode for Ar^+, Ar^{2+}, N^+, N_2^+, Ta^+, Ta^{2+}, Ti^+, and Ti^{2+} while sputtering in Ar/N_2 gas mixtures under the same conditions of

pressure and gas flow rates as used for the film growth experiments. More details can be found in Ref. 29.

Ti$_{1-x}$Ta$_x$N film compositions x are determined by EDS measurements carried out on fracture cross-sections. N/(Ti + Ta) fractions are obtained by Rutherford backscattering spectroscopy (RBS) using a 2.0 MeV ^{4}He$^+$ probe beam incident at 10° with respect to the surface normal and detected at a 172° scattering angle. Experimental data are analyzed based upon SIMNRA 6.06 software.[30] Film thicknesses are determined from XSEM analyses in a LEO 1550 instrument.

θ-2θ x-ray diffraction (XRD) scans in 2θ steps of 0.1°, XRR, and sin$^2\psi$ measurements for residual stress determinations,[31] are carried out using a Philips X'Pert MRD system operated with point-focus Cu Kα radiation. Relaxed TiN and Ti$_{0.92}$Ta$_{0.08}$N lattice parameters a_o are determined from θ-2θ scans acquired at the strain-free tilt angle ψ^* defined as $\psi^* = \arcsin[(2\nu/(1 + \nu))^{1/2}]$,[19] in which ν is the Poisson ratio.

The sin$^2\psi$ method employs Hooke's law of linear elasticity expressed as[31]

$$\varepsilon(\psi) = \frac{1 + \nu}{E}\sigma \sin^2\psi - \frac{2\nu}{E}\sigma, \tag{1}$$

for which ν is the Poisson ratio and ε is the film strain obtained from

$$\varepsilon(\psi) = \frac{d_\psi - d_0}{d_0}. \tag{2}$$

Lattice spacings d_ψ in Eq. (2) are determined for each sample from the positions of the cubic 111 Bragg reflections at ten different values of the tilt angle ψ ranging from 0 to 71.57°, with ψ steps that produce equally spaced data points on the sin$^2\psi$ axis. The relaxed interplanar spacing d_o is acquired at the strain-free tilt angle ψ^*;[31] elastic moduli E inserted in Eq. (1) are obtained from nanoindentation measurements (Fig. 7); and Poisson ratios, $\nu = 0.25$ for TiN and 0.23 for Ti$_{0.92}$Ta$_{0.08}$N, are from Refs. 32 and 33, respectively.

Plan-view transmission electron microscopy (TEM) and XTEM specimens are prepared by mechanical polishing, followed by several hours of Ar$^+$ ion milling at 5 kV with an 8° incidence angle and sample rotation. During the final stages (10–20 min) of sample thinning, the ion energy and incidence angle are reduced to 2.5 kV and 5°. Film nanostructures are analyzed in an FEI Tecnai G2 TF 20 UT transmission electron microscope operated at 200 kV.

X-ray photoelectron spectroscopy (XPS) compositional depth profiles of as-deposited films are acquired in a Axis Ultra DLD instrument from Kratos Analytical using monochromatic Al Kα radiation (hν = 1486.6 eV). The results serve as a qualitative measure of film density and are consistent with XTEM analyses, since highly underdense layers exhibit significant oxygen concentrations throughout the film following air exposure. Ar$^+$ sputter etching at 4 keV and 12.7 mA/cm^2, an incident angle of 70° with respect to the sample normal, and

with the beam rastered over a 3×3 mm^2 area, is performed in one-minute steps, corresponding to the removal of 160 Å/step as determined by XSEM fracture cross-section calibrations. The area analyzed by XPS is 0.3×0.7 mm^2 and centered in the middle of the ion-etched crater.

A sharp Berkovich diamond tip is used to determine nanoindentation hardness H and elastic moduli E of all films, both reference samples and Ta-HIPIMS/Ti-DCMS layers, following the procedure of Oliver and Pharr.[34] A minimum of 20 indents, with a maximum load of 15 mN, are made in each sample. Indentation depths range from 1500 to 2000 Å, but are never allowed to exceed 10% of the film thickness in order to minimize substrate effects.

Transport of ions in matter (TRIM),[35] a Monte Carlo program included in the stopping power and range of ions in matter (SRIM) software package,[36] is used to estimate primary-ion and recoil projected ranges due to Ta^{n+} and Ti^{n+} metal–ion irradiation during Ti$_{1-x}$Ta$_x$N and TiN film growth.

III. RESULTS

A. Mass and energy spectroscopy analyses

In situ mass spectrometry and energy spectroscopy measurements reveal the presence of large fluxes of energetic Ta$^+$ and Ta^{2+} metal–ions incident at the substrate position during Ta-HIPIMS pulses. Figures 1(a) and 1(b) show Ta$^+$ and Ta^{2+} IEDFs acquired during 200 μs metal–ion HIPIMS pulses (from $t_{\text{offset}} = 80\ \mu$s to $t = 280\ \mu$s) with energy E_p varied from 3 to 18 J in steps of 3 J. For singly ionized Ta$^+$, the primary effect of increasing E_p is an increase in the average ion energy, from 4.9 eV with $E_p = 3$ J to 9.9 eV with $E_p = 18$ J, due to increasing intensities in the high-energy tails. The maximum Ta$^+$ ion intensity increases from 1.2×10^6 to 3.2×10^6 cps. The average energy of Ta^{2+} ions ranges from 7.6 eV with $E_p = 3$ J to 8.5 and 9.8 eV with $E_p = 12$ and 18 J as the maximum flux intensity increases from 3.5×10^5 to 4.1×10^6 and 3.1×10^6 cps. The doubly ionized Ta^{2+} fraction Ta^{2+}/(Ta$^+$ + Ta^{2+}) in the metal–ion flux incident at the film growth surface during HIPIMS pulses increases from 0.33 with $E_p = 3$ J to 0.45 at 18 J. With $E_p = 5$ J, the pulse energy used for growth of Ti$_{0.92}$Ta$_{0.08}$N films, Ta^{2+}/(Ta$^+$ + Ta^{2+}) = 0.36.

Time-resolved measurements during HIPIMS pulses show that with a pulse energy $E_p = 5$ J, the first Ta$^+$ ions reach the substrate plane at $t = 60\ \mu$s with a mean energy of $\sim$20 eV, corresponding to a flight time of 28 μs. Thus, sputtering of the Ta target begins at $t \sim 30\ \mu$s after pulse initiation. The metal–ion flux at the substrate increases with time into the pulse and at $t = 80\ \mu$s exceeds that of the inert-gas ions. The maximum Ta$^+$ flux J_{Ta^+} is obtained near $t = 130\ \mu$s. At longer times, J_{Ta+} decreases slowly until at $t > 280\ \mu$s, inert-gas ions again dominate the ion flux to the substrate. Doubly charged Ta^{2+} ions are predominantly produced during the most energetic phase of the discharge. $J_{\text{Ta}^{2+}}$ at the substrate reaches a maximum near $t = 120\ \mu$s.

Corresponding Ti$^+$ and Ti^{2+} metal-ion fluxes incident at the substrate position during Ti-HIPIMS/Ti-DCMS TiN film growth are shown for reference in Figs. 1(c) and 1(d).
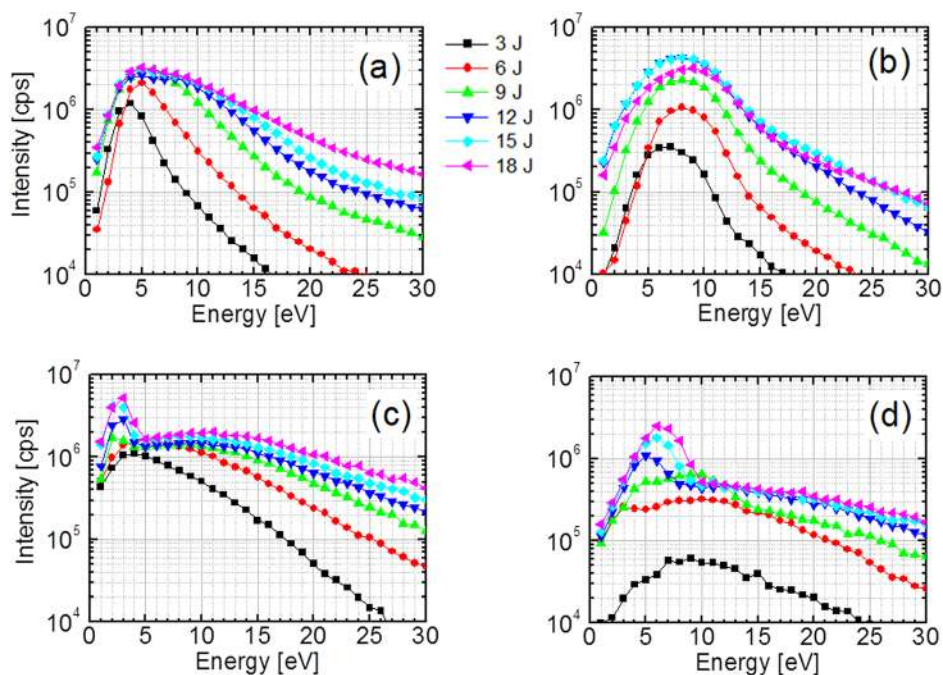
FIG. 1. (Color online) IEDFs for: (a) Ta^+, (b) Ta^{2+}, (c) Ti^+, and (d) Ti^{2+} metal–ions, incident at the substrate position, from Ta and Ti targets powered by HIPIMS as a function of pulse energy E_p.

Ti^{n+} and Ta^{n+} IEDF shapes differ significantly. This is particularly obvious at $E_p \geq 12$ J, for which high-intensity peaks, with relatively narrow energy distributions, appear at low energies superimposed on the broad IEDFs. The low-energy peaks arise due to Ti^+ and Ti^{2+} ions being more efficiently thermalized than their high-mass Ta^+/Ta^{2+} counterparts during transport through the plasma. That is, the mass match between Ti (47.87 amu) and Ar (39.95 amu) is much better than for Ta (180.95) and Ar. The Ti^{2+} fraction $Ti^{2+}/(Ti^+ + Ti^{2+})$ in the metal-ion flux incident at the growing film surface ranges from 0.08 with $E_p = 3$ J to 0.30 with $E_p = 18$ J. Ti-HIPIMS/Ti-DCMS TiN reference layers are grown with $E_p = 5$ J, for which $Ti^{2+}/(Ti^+ + Ti^{2+}) = 0.12$.

Previous mass spectroscopy results for Ti-DCMS, under the same deposition conditions as employed here, reveal that the ion flux incident at the growing film is dominated by low-energy gas species (primarily Ar^+ and N_2^+).[19] Average ion energies are 2.3 eV for Ar^+ (84% of the ion flux) and 2.8 eV for N_2^+ (4.9%). Ti^+ ions have higher energies, 4.8 eV, but account for only 10% of the ion flux incident at the substrate plane, while the Ar^{2+}, Ti^{2+}, and N^+ ion fluxes are slightly higher than the detection limit and constitute 0.8, 0.2, and 0.1% of the total ion flux, respectively.

B. $Ti_{1-x}Ta_xN$ film composition

The concentration x of TaN in $Ti_{1-x}Ta_xN$ films increases from $x = 0.08$ with $E_p = 5$ J, to 0.13 and 0.16 with $E_p = 10$ and 15 J, respectively. $Ti_{1-x}Ta_xN$ alloys grown with $E_p = 5$ J and substrate biases $V_s = 20 - 280$ V applied in synchronous with the metal–ion rich portions of Ta-HIPIMS pulses are found to be of constant composition with $x = 0.08$. RBS analyses indicate that $N/(Ta + Ti) = 1.00 \pm 0.03$ for all $Ti_{1-x}Ta_xN$ alloys.

C. Nanostructure

As shown in Secs. III D and III E, the optimum combination of high hardness and elastic modulus in fully dense films with essentially zero residual stress is obtained for Ta-HIPIMS/Ti-DCMS $Ti_{0.92}Ta_{0.08}N$ layers grown with $V_s = 160$ V. Thus, we primarily concentrate on these alloys for comparison to TiN reference layers grown by DCMS and Ti-HIPIMS/Ti-DCMS.

Figure 2 shows three sets of ψ-2θ scans as a function of the tilt angle ψ, defined as the angle between the surface normal and the diffraction plane containing the incoming and diffracted x-ray beams, for (a) DCMS TiN films deposited with $V_s = 10$ V, (b) Ta-HIPIMS/Ti-DCMS $Ti_{0.92}Ta_{0.08}N$ films grown with metal–ion-synchronized substrate bias $V_s = 160$ V, and (c) Ti-HIPIMS/Ti-DCMS TiN layers grown as in (b) with $V_s = 160$ V. There is no applied heating in the three sets of growth experiments and the maximum temperature during deposition, due to plasma heating, is $\leq 120\,^\circ C$ (see the Appendix). The only peaks observed in the ψ-2θ scans are cubic NaCl-structure 111 and 002 reflections. Thus, we focus in Fig. 2 on the 2θ region between 33 and 47°, which includes both peaks. The tilt angle ψ is varied from 0 to 71.6° such that $\sin^2\psi$ ranges from 0 to 0.9 in steps of 0.1.

For DCMS TiN films, the 002 peak position obtained at the strain-free tilt angle, $\psi^* = 39.2°$, is 42.51° corresponding to a relaxed lattice parameter $a_o = 4.25 \pm 0.01$ Å, essentially equal to TiN powder diffraction data.[37] The 111 and 002 peak positions do not change significantly as a function of the tilt angle ψ, indicative of low residual stress. Normalizing peak intensities to those obtained from powder diffraction,[37] reveals that DCMS TiN films have very strong 111 preferred orientation.
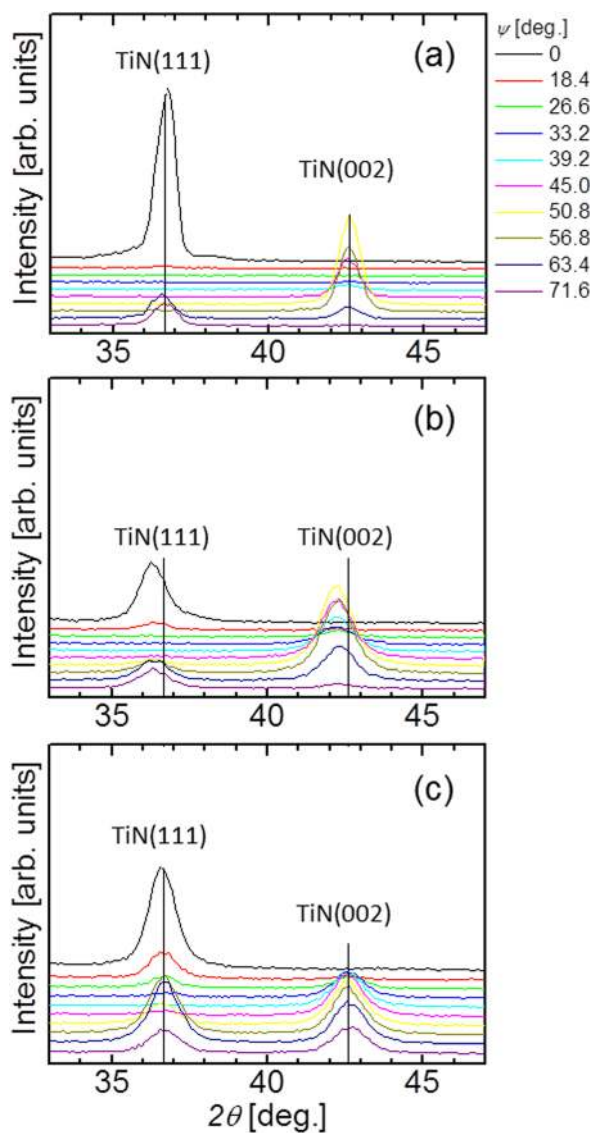
FIG. 2. (Color online) ψ-2θ scans for: (a) DCMS TiN films grown with $V_s = 10$ V, (b) Ta-HIPIMS/Ti-DCMS $Ti_{0.92}Ta_{0.08}N$ films grown with $V_s = 160$ V, and (c) Ti-HIPIMS/Ti-DCMS TiN layers with $V_s = 160$ V. For both (b) and (c), the bias is synchronized with the metal–ion rich portions of HIPIMS pulses. In all three cases, there is no external substrate heating ($T_s \leq 120\,^\circ$C) during film growth on Si(001) substrates. The vertical lines in each panel designate the positions of TiN reflections from reference powder diffraction data (Ref. 37).

The 111 and 002 diffraction peaks from Ta-HIPIMS/Ti-DCMS $Ti_{0.92}Ta_{0.08}$ N alloys are broader [see Fig. 2(b)], exhibit reduced intensity, and are shifted to lower 2θ values compared to DCMS TiN layer results in Fig. 2(a). The strain-free ($\psi = 39.2^\circ$) $Ti_{0.92}Ta_{0.08}$ N 002 XRD peak position is 42.24°, compared to 42.51° for DCMS TiN, resulting in a larger relaxed lattice parameter, $a_o = 4.28 \pm 0.01$ Å, which is independent of the synchronous substrate bias V_s. As was the case for DCMS TiN, Ta-HIPIMS/Ti-DCMS $Ti_{0.92}Ta_{0.08}$ N 111 and 002 peak positions do not shift significantly as a function of ψ, indicative of low film stresses; the alloys exhibit 111 preferred orientation.

The Ti-HIPIMS/Ti-DCMS TiN film strain-free 002 XRD peak position in Fig. 2(c) is 42.63° yielding a relaxed lattice

parameter $a_o = 4.24 \pm 0.01$ Å, close to that of DCMS TiN (4.25 ± 0.01 Å). These films also exhibit low residual stresses with 111 preferred orientation.

1. TiN/$Ti_{0.92}Ta_{0.08}$N/TiN trilayers

Figure 3 is a bright-field XTEM image of a trilayer (DCMS TiN)/(Ta-HIPIMS/Ti-DCMS $Ti_{0.92}Ta_{0.08}$ N)/(DCMS TiN) sample grown on a Si(001) wafer without external heating. The layer thicknesses are 8700, 9300, and 8250 Å; the $Ti_{0.92}Ta_{0.08}$ N alloy layer is deposited with $E_p = 5$ J; and a metal–ion-synchronized substrate bias $V_s = 160$ V. DCMS TiN layers are grown with the substrate electrically floating,
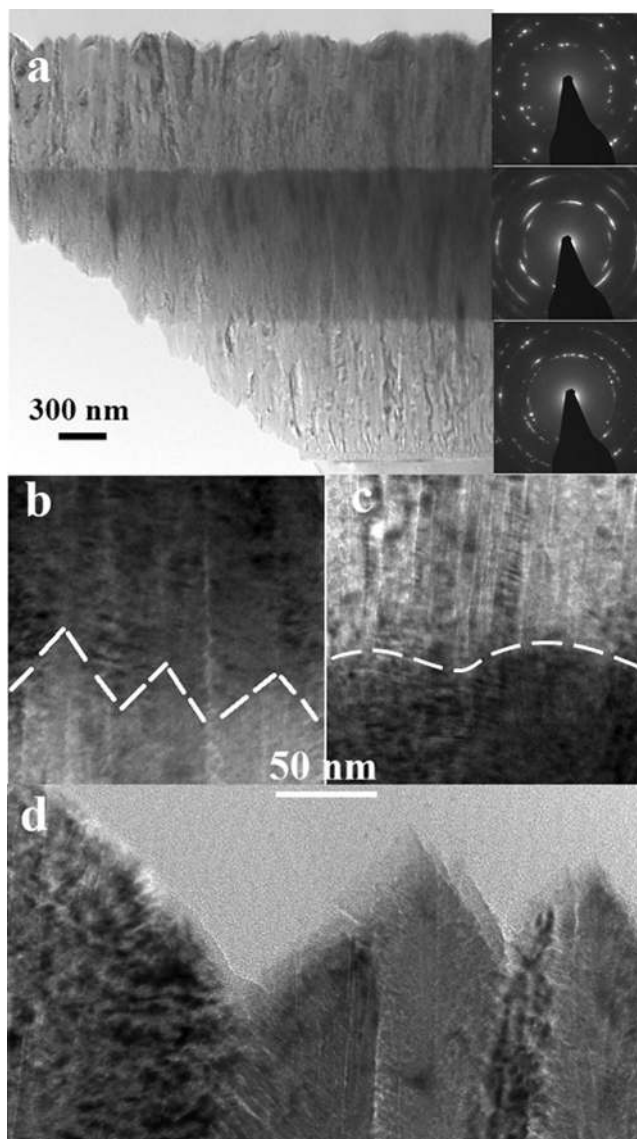

FIG. 3. (a) Bright-field XTEM image of a trilayer (DCMS TiN)/(Ta-HIPIMS/Ti-DCMS $Ti_{0.92}Ta_{0.08}$N)/(DCMS TiN) film grown without external heating. The Si(001) substrate is electrically floating, $V_s = 10$ V, during TiN deposition; while for alloy growth, $V_s = 160$ V synchronized to the metal–ion-rich portions of HIPIMS pulses. SAED patterns from each layer are shown as insets. Higher-resolution XTEM images are also presented highlighting (b) the interface between the lower DCMS TiN layer and the Ta-HIPIMS/Ti-DCMS $Ti_{0.92}Ta_{0.08}$N alloy, (c) the interface between the Ta-HIPIMS/Ti-DCMS $Ti_{0.92}Ta_{0.08}$N alloy film and the upper DCMS TiN film, and (d) the top surface of the trilayer sample.

$V_s = V_f = 10$ V. Image contrast between $Ti_{0.92}Ta_{0.08}$N and the two TiN encapsulation layers is due to enhanced electron absorption by the heavier Ta atoms combined with the higher density (see below) of the Ta-HIPIMS/Ti-DCMS film.

The DCMS TiN underlayer in Fig. 3 has a columnar nanostructure and pronounced intercolumnar voids. The average column diameter is 100 ± 20 Å near the substrate and increases to 570 ± 160 Å at the top of the layer. The columns also exhibit an intracolumnar network of voids [see Fig. 3(b)], with typical size <10 Å. This is a signature of low adatom surface mobilities.[3,38] XTEM and XSEM images reveal that the 111-oriented TiN columns have conical upper surfaces with sharp tips and an average peak-to-valley distance w of 300 ± 100 Å. From plan-view images, the cones are approximately symmetric. The layer roughness results from kinetic roughening due to the presence of step-edge Ehrlich barriers[39,40] on locally epitaxial column surfaces. The roughening rate is exacerbated by atomic shadowing arising from the combination of an approximately cosine point emission pattern from the target[41–44] and gas-phase scattering.[45]

The increase in film density between the lower TiN and middle $Ti_{0.92}Ta_{0.08}$N layer is clearly shown in the higher-resolution XTEM image in Fig. 3(b) and consistent with XRR results in Sec. III C 2. Columnar growth is preserved; the average column diameter is 570 ± 120 Å at the bottom of the alloy layer, close to the average column size in the upper region of the underlying DCMS TiN layer, suggesting local epitaxy. The intracolumnar voids disappear within the first 100 Å into the $Ti_{0.92}Ta_{0.08}$N layer due to pulsed Ta^+/Ta^{2+} metal–ion irradiation-induced atomic mixing. However, the intercolumnar voids persist for $500–1000$ Å because of low adatom mean-free-paths compared to average feature sizes. Figure 3(c) reveals that the $Ti_{0.92}Ta_{0.08}$N surface is much smoother than that of the TiN underlayer; the column tops have become rounded and shallower with an average peak-to-valley distance that has decreased by approximately a factor of two to $w = 150 \pm 50$ Å. The average column diameter at the top of the 9300-Å-thick Ta-HIPIMS/Ti-DCMS $Ti_{0.92}Ta_{0.08}$N interlayer is 1980 ± 200 Å, an increase by a factor of 3.5×.

Figure 3(c) also shows that intercolumnar porosity reappears, within less than 50 Å, during growth of the upper DCMS TiN layer with $V_s = 10$ V. The rough surface and associated intercolumnar porosity observed in the DCMS TiN underlayer [Figs. 3(a) and 3(b)] also develop as shown in Fig. 3(d), an XTEM image of the surface region of the tri-layer film. The average column diameter of the 8250 Å-thick upper DCMS TiN film is 80 ± 20 Å near the interface with the $Ti_{0.92}Ta_{0.08}$N interlayer and increases to 680 ± 260 Å in the surface region. The average peak-to-valley roughness is 500 ± 300 Å.

Corresponding selected area electron diffraction (SAED) patterns acquired from the middle portions of each layer of the TiN/$Ti_{0.92}Ta_{0.08}$N/TiN sample are shown as insets in Fig. 3. All layers exhibit 111 texture in agreement with the XRD results presented above.

2. Single layers

Figure 4 compares fracture XSEM images acquired near the top of a 1.95 μm-thick DCMS TiN reference film deposited with $V_s = 10$ V [Fig. 4(a)] and a 1.85 μm-thick $Ti_{0.92}Ta_{0.08}$N Ta-HIPIMS/Ti-DCMS alloy layer grown with a metal–ion-synchronized bias $V_s = 160$ V [Fig. 4(b)]. In both cases, $T_s \leq 120\,°C$ (see the Appendix). The TiN reference sample is characterized by conical column tops with an average peak-to-valley distance $w = 700$ Å; the film fractures in an intercolumnar manner and the side walls of the pillars exhibit nanostructure, which corresponds to nanoporosity within the columns as observed by XTEM [Fig. 3(d)]. The surfaces of the $Ti_{0.92}Ta_{0.08}$N Ta-HIPIMS/Ti-DCMS films are much flatter exhibiting mounded structures with heights $50–100$ Å, shallow troughs at boundaries, and no discernable porosity. The cross-sectional image reveals mixed inter- and intracolumnar fracture.

Figure 5 shows XPS oxygen concentration depth profiles $C_O(h)$ acquired over the first 5000 Å from the surface of air-exposed layers: (a) a Ref. DCMS TiN film grown with $V_s = V_f = 10$ V, (b) a Ti-HIPIMS/Ti-DCMS TiN layer, and (c) a Ta-HIPIMS/Ti-DCMS $Ti_{0.92}Ta_{0.08}$N alloy layer. Both films (b) and (c) were grown with a metal–ion synchronized bias of 160 V. C_O for the DCMS TiN film, after removal of the surface native oxide layer, saturates at a value of ~ 8 at. % with $h \gtrsim 1000$ Å. This is a sign of an underdense microstructure. The oxygen concentration profile for the Ti-HIPIMS/Ti-DCMS TiN layer deposited with
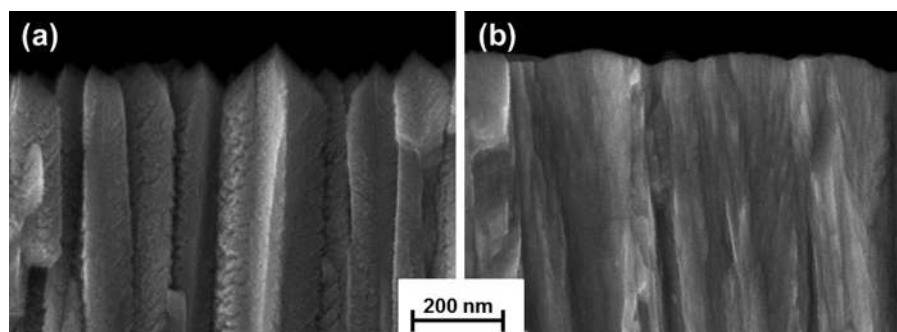

FIG. 4. Cross-sectional SEM images of the area near the top of (a) a DCMS TiN reference film grown on Si(001) with $V_s = 10$ V and (b) a Ta-HIPIMS/Ti-DCMS $Ti_{0.92}Ta_{0.08}$N alloy layer grown on Si(001) with $V_s = 160$ V synchronized to the metal-ion-rich portions of HIPIMS pulses. In both cases, there is no external substrate heating ($T_s \leq 120\,°C$) during film growth.
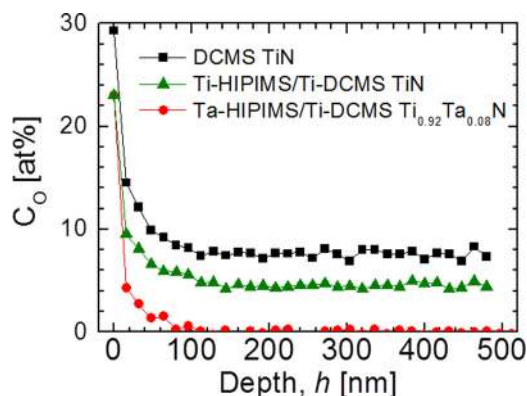
FIG. 5. (Color online) XPS oxygen concentration depth profiles $C_O(h)$ from the air-exposed surface through the first 5000 Å of (a) a reference DCMS TiN film grown with $V_s = 10$ V, (b) a Ti-HIPIMS/Ti-DCMS TiN layer grown with $V_s = 160$ V, and (c) a Ta-HIPIMS/Ti-DCMS Ti$_{0.92}$Ta$_{0.08}$N alloy layer grown with $V_s = 160$ V. For the films in (b) and (c), the applied bias is synchronized with the metal–ion-rich portions of HIPIMS pulses. In all three cases, there is no external substrate heating ($T_s \leq 120\,^{\circ}$C) during film growth on Si(001) substrates.

synchronized Ti$^+$/Ti^{2+} metal–ion irradiation pulses is very similar to that of the DCMS TiN film, but with a lower bulk concentration of ∼5 at. %, indicative of lower porosity. In contrast, the bulk film C_O value for Ti$_{0.92}$Ta$_{0.08}$N alloy films grown with synchronized Ta$^+$/Ta^{2+} metal–ion bombardment pulses is less than the oxygen detection limit, ∼1 at. %, indicating a dense nanostructure, consistent with cross-sectional electron microscopy images in Figs. 3 and 4.

We quantify the density of representative single-layer films using XRR and a stoichiometric, single-crystal TiN/MgO(001) reference sample.[46] DCMS TiN layers deposited with $T_s < 120\,^{\circ}$C and $V_s = 10$ V have a relative density of 65%. The density of Ta-HIPIMS/Ti-DCMS Ti$_{0.92}$Ta$_{0.08}$N layers grown with $V_s = 20$ V is 76% (relative to 6.14 g/cm^3 for a fully dense alloy film with 8 mol. % TaN and a_o = 4.28 Å), while Ta-HIPIMS/Ti-DCMS Ti$_{0.92}$Ta$_{0.08}$N layers grown with $V_s = 160$ V exhibit a density of 98%.

Optical photographs show that DCMS TiN reference films grown with $V_s = 10$ V exhibit a dark brown appearance typical of films deposited at low temperature ($T_s/T_m < 0.12$ in this case, where T_m is the melting temperature) and, hence, have high surface roughness resulting in light trapping and low reflectivity. Ti$_{0.92}$Ta$_{0.08}$N Ta-HIPIMS/Ti-DCMS alloy layers grown with metal–ion synchronized bias $V_s = 160$ V are golden in color with a shiny reflective surface.

D. Nanoindentation hardness and elastic moduli

Nanoindentation hardness H and elastic moduli E of Ti$_{0.92}$Ta$_{0.08}$N films, deposited with no external heating ($T_s \leq 120\,^{\circ}$C), are plotted in Figs. 6 and 7 as a function of the applied substrate bias voltage V_s synchronized to the metal–ion portions of the HIPIMS pulses. Results are also shown for four sets of reference layers: (1) DCMS TiN deposited with $T_s < 120\,^{\circ}$C and $V_s = 10$ V, (2) DCMS TiN grown at $T_s = 500\,^{\circ}$C with continuously applied bias, $V_s = 60$ V, (3) Ti-HIPIMS/Ti-DCMS TiN layers deposited at $T_s \leq 120\,^{\circ}$C with substrate bias $20 \leq V_s \leq 280$ V synchronized to the
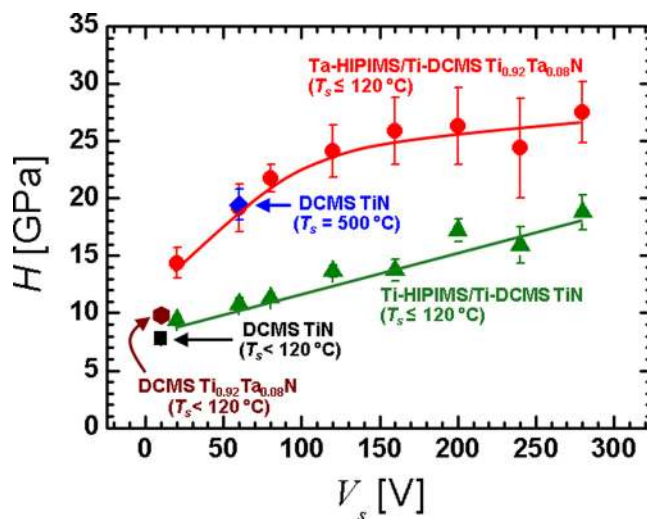

FIG. 6. (Color online) Hardness H of Ta-HIPIMS/Ti-DCMS Ti$_{0.92}$Ta$_{0.08}$N/Si(001) films as a function of the applied substrate bias voltage V_s synchronized to the metal-ion-rich portions of HIPIMS pulses. Results are also shown for four sets of reference layers grown on Si(001) substrates: (1) DCMS TiN deposited with $V_s = 10$ V, (2) DCMS TiN grown at $T_s = 500\,^{\circ}$C with $V_s = 60$ V, (3) Ti-HIPIMS/Ti-DCMS TiN films deposited with synchronized substrate bias $20 \leq V_s \leq 280$ V, and (4) DCMS Ti$_{0.92}$Ta$_{0.08}$N alloys grown at $T_s < 120\,^{\circ}$C with $V_s = 10$ V. Except for TiN reference layer (2), there is no external substrate heating and $T_s \leq 120\,^{\circ}$C.

metal–ion rich portions of the HIPIMS pulses, and (4) DCMS Ti$_{0.92}$Ta$_{0.08}$N alloys grown at $T_s < 120\,^{\circ}$C with $V_s = 10$ V.

H for DCMS TiN reference layers grown with no external heating and $V_s = 10$ V is very low, 7.8 GPa, as expected due to the underdense nanostructure (see Figs. 3–5), and only marginally higher, 9.8 GPa, for DCMS Ti$_{0.92}$Ta$_{0.08}$N alloy films. The DCMS TiN layer grown at 500 °C has hardness $H = 19.4$ GPa, similar to values reported for epitaxial
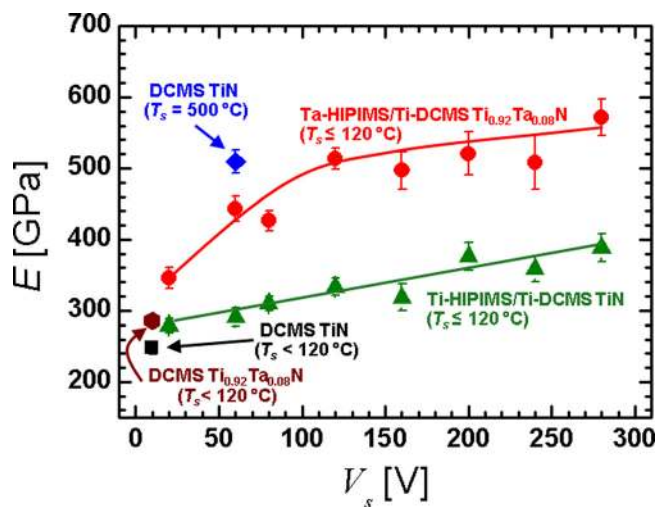

FIG. 7. (Color online) Elastic moduli E of Ta-HIPIMS/Ti-DCMS Ti$_{0.92}$Ta$_{0.08}$N/Si(001) films as a function of the applied substrate bias voltage V_s synchronized to the metal-ion-rich portions of HIPIMS pulses. Results are also shown for four sets of reference layers grown on Si(001) substrates: (1) DCMS TiN deposited with $V_s = 10$ V, (2) DCMS TiN grown at $T_s = 500\,^{\circ}$C with $V_s = 60$ V, (3) Ti-HIPIMS/Ti-DCMS TiN films deposited with synchronized substrate bias $20 \leq V_s \leq 280$ V, and (4) DCMS Ti$_{0.92}$Ta$_{0.08}$N alloys grown at $T_s < 120\,^{\circ}$C with $V_s = 10$ V. Except for TiN reference layer (2), there is no external substrate heating and $T_s \leq 120\,^{\circ}$C.

TiN(001).[47,48] For Ti-HIPIMS/Ti-DCMS, TiN films grown with $V_s = 20$ V, H is low and equal to 9.4 GPa. With increasing V_s, Ti-HIPIMS/Ti-DCMS TiN films exhibit a linear increase in hardness to 18.8 GPa at $V_s = 280$ V. Ta-HIPIMS/Ti-DCMS Ti$_{0.92}$Ta$_{0.08}$N layers grown with $V_s = 20$ V have a hardness of 14.4 GPa, almost twice that of low-T_s DCMS TiN. Increasing V_s to 60, 80, and 120 V, results in further increases in H to 19.1, 21.8, and 24.1 GPa, respectively. At still higher synchronized biases, $160 \leq V_s \leq 280$ V, H remains relatively constant at 26 ± 1.3 GPa.

The results presented in Fig. 6 indicate that even a small dose of heavy-metal–ion bombardment per HIPIMS pulse has a large effect on film properties. Synchronized $V_s = 160$ V metal–ion bombardment with Ta$^+$/Ta^{2+} ions during Ta-HIPIMS/Ti-DCMS Ti$_{0.92}$Ta$_{0.08}$N deposition results in layers with significantly higher hardness, 25.9 GPa, than that of Ti-HIPIMS/Ti-DCMS TiN films grown with Ti$^+$/Ti^{2+} ion irradiation pulses, 13.8 GPa, using the same HIPIMS conditions (5 J/p, 100 Hz, and 2% duty cycle). The hardness of Ti-HIPIMS/Ti-DCMS TiN layers grown with $V_s = 20$ V is only 9.4 GPa, i.e., comparable to low-T_s TiN DCMS film, both significantly lower than for Ta-HIPIMS/Ti-DCMS Ti$_{0.92}$Ta$_{0.08}$N layers. With increasing synchronous substrate bias, Ti-HIPIMS/Ti-DCMS TiN films exhibit a linear increase in H. However, over the entire substrate bias range, $20 \leq V_s \leq 280$ V, Ta-HIPIMS/Ti-DCMS Ti$_{0.92}$Ta$_{0.08}$N alloys have hardness, which are 50–70% higher than Ti-HIPIMS/Ti-DCMS layers.

The trends in elastic moduli E dependences on x and V_s (see Fig. 7) follow the hardness results described above. For DCMS TiN films, E increases from 248 GPa for films grown with $T_s < 120\,°$C and $V_s = 10$ V to $E = 509$ GPa with $T_s = 500\,°$C and $V_s = 60$ V. The latter is close to previously reported values for epitaxial TiN(001).[47,48] For DCMS, Ti$_{0.92}$Ta$_{0.08}$N films deposited with no external heating and floating bias, $E = 286$ GPa. Ta-HIPIMS/Ti-DCMS Ti$_{0.92}$Ta$_{0.08}$N alloys grown with no external heating and the lowest applied synchronized substrate bias, $V_s = 20$ V, have moduli $E = 346$ GPa, a 40% increase with respect to low-T_s DCMS TiN values. Raising V_s results in an additional increase in E to 443 GPa with $V_s = 60$ V and 497 GPa with $V_s = 160$ V. E does not increase significantly with further increases in V_s to 280 V.

The elastic moduli of Ti-HIPIMS/Ti-DCMS TiN films grown with metal–ion-synchronized Ti$^+$/Ti^{2+} irradiation and $T_s \leq 120\,°$C exhibit a linear increase with V_s (Fig. 7) from 279 GPa with $V_s = 20$ V to 388 GPa with $V_s = 280$ V, but remain 25 to 35% lower than corresponding values for Ta-HIPIMS/Ti-DCMS Ti$_{0.92}$Ta$_{0.08}$N layers deposited with the same V_s.

Ta-HIPIMS/Ti-DCMS Ti$_{1-x}$Ta$_x$N films with higher TaN concentrations, $x = 0.13$ and 0.16, have higher hardness and elastic moduli values than Ti$_{0.92}$Ta$_{0.08}$N alloys for a given V_s. $H = 23$ GPa for Ti$_{0.87}$Ta$_{0.13}$N grown with metal–ion-synchronized $V_s = 20$ V pulses and increases to 27.8 and 30.8 GPa with $V_s = 60$ and 80 V. Correspondingly, E for Ti$_{0.87}$Ta$_{0.13}$N layers increases from 435 to 540 and 611 GPa with $V_s = 20$, 60, and 80 V. $H = 26$ GPa and $E = 517$ GPa for Ti$_{0.84}$Ta$_{0.16}$N layers grown with $V_s = 20$ V, increasing to 30.5 and 603 GPa with $V_s = 60$ V. However, the increase in H and E values with increasing x is accompanied by higher compressive stresses, as shown in Sec. III E.

E. Residual stress

Residual stress values σ, obtained from $\sin^2\psi$ analyses, for Ta-HIPIMS/Ti-DCMS Ti$_{0.92}$Ta$_{0.08}$N films are plotted as a function of synchronized pulsed bias voltage V_s in Fig. 8. Results are also shown for the four sets of reference layers described in Secs. II and III D.

The data presented in Fig. 8 are corrected for the tensile differential thermal contraction stress σ_{th}, which arises during cooling of the samples from T_s (see Fig. 11 in the Appendix) to room temperature, ΔT. σ_{th} is given by[49]

$$\sigma_{th} = \frac{E(\alpha_f - \alpha_s)\Delta T}{1 - \nu}, \tag{3}$$

for which α_f and α_s are the film and substrate thermal expansion coefficients.

The average thermal expansion coefficient of Si(001) over the temperature range from 120 to 23 °C is $\alpha_s = 2.9 \times 10^{-6}$ K^{-1}.[50] Since α_f for Ti$_{1-x}$Ta$_x$N films is unknown, we use a linear extrapolation between $\alpha_{TiN} = 9.35 \times 10^{-6}$ K^{-1} and $\alpha_{TaN} = 8.00 \times 10^{-6}$ K^{-1} from Ref. 51 to obtain $\alpha_{Ti_{0.92}Ta_{0.08}N} = 9.24 \times 10^{-6}$ K^{-1} for Ti$_{0.92}$Ta$_{0.08}$N. σ_{th} ranges from -0.25 GPa for Ti$_{0.92}$Ta$_{0.08}$N grown with $V_s = 20$ V to -0.35 GPa for Ti$_{0.92}$Ta$_{0.08}$N deposited with $V_s = 280$ V; for reference DCMS and Ti-HIPIMS/Ti-DCMS layers grown with no external heating and the same V_s range, σ_{th} varies from -0.23 to -0.32 GPa, while for the reference TiN film grown at $T_s = 500\,°$C with $V_s = 10$ V, $\sigma_{th} = -1.6$ GPa.
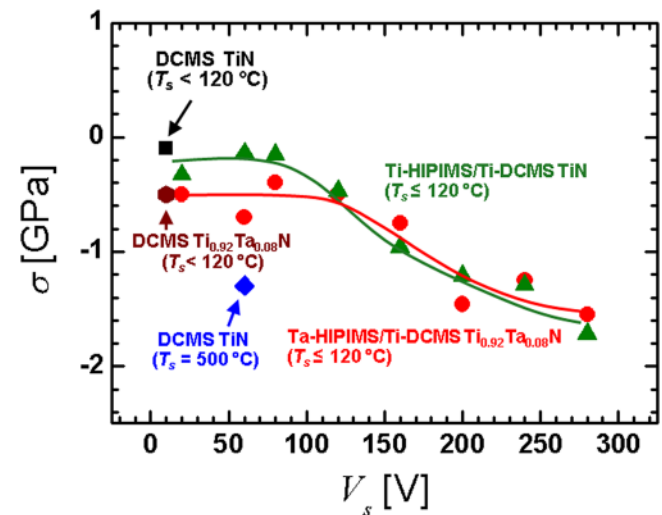

FIG. 8. (Color online) Residual stress σ for Ta-HIPIMS/Ti-DCMS Ti$_{0.92}$Ta$_{0.08}$N/Si(001) films as a function of the applied substrate bias voltage V_s synchronized to the metal–ion-rich portions of HIPIMS pulses. Results are also shown for four sets of reference layers grown on Si(001) substrates: (1) DCMS TiN deposited with $V_s = 10$ V, (2) DCMS TiN grown at $T_s = 500\,°$C with $V_s = 60$ V, (3) Ti-HIPIMS/Ti-DCMS TiN films deposited with synchronized substrate bias $20 \leq V_s \leq 280$ V, and (4) DCMS Ti$_{0.92}$Ta$_{0.08}$N alloys grown at $T_s < 120\,°$C with $V_s = 10$ V. Except for TiN reference layer (2), there is no external substrate heating and $T_s \leq 120\,°$C.

Underdense DCMS TiN reference layers grown with no external heating and $V_s = 10$ V are essentially stress-free, $\sigma = -0.1$ GPa, but DCMS TiN layers grown at 500 °C have a compressive stress of -1.3 GPa. DCMS $Ti_{0.92}Ta_{0.08}N$ layers grown with no external heating and $V_s = 10$ V also exhibit low stress, $\sigma = -0.5$ GPa. For $Ti_{0.92}Ta_{0.08}N$ alloys deposited with no external heating and synchronous bias $V_s \leq 160$ V, residual stresses are small, ranging from $\sigma = -0.5$ GPa with $V_s = 20$ V to -0.4 GPa with $V_s = 80$ V to -0.7 GPa with $V_s = 160$ V. With $V_s \geq 200$ V, σ for $Ti_{0.92}Ta_{0.08}N$ increases to -1.4 ± 0.15 GPa.

Ti-HIPIMS/Ti-DCMS TiN films grown with Ti^+/Ti^{2+} ion irradiation, $V_s \leq 120$ V, and no external heating are essentially stress free. At higher synchronous biases, residual stresses become compressive and increase from -1.0 GPa with $V_s = 160$ V to -1.2, -1.3, and -1.7 GPa with $V_s = 200$, 240, and 280 V.

Residual stresses in $Ti_{1-x}Ta_xN$ alloys, deposited with no external heating, increase with increasing TaN concentration. $\sigma = -0.7$ GPa for $Ti_{0.87}Ta_{0.13}N$ films grown with $V_s = 20$ V and increases rapidly to -1.6 and -2.1 GPa with $V_s = 60$ and 80 V. Even higher stress values are obtained in $Ti_{0.84}Ta_{0.16}N$ layers, $\sigma = -1.4$ for alloys deposited with $V_s = 20$ V and -2.8 GPa with $V_s = 60$ V.

IV. DISCUSSION

DCMS TiN films deposited at $T_s < 120$ °C ($T_s/T_m \leq 0.12$) with $V_s = 10$ V exhibit pronounced inter- and intracolumnar porosity (see XTEM and XSEM images in Figs. 3 and 4) due to low adatom mobilities, which give rise to kinetic surface roughening[52–54] exacerbated by atomic shadowing.[55] The severe underdensity (65% dense, based upon XRR results) results in very low hardness, $H = 7.8$ GPa, and elastic modulus, $E = 248$ GPa, values.

The addition of pulsed heavy-metal Ta^+/Ta^{2+} ion irradiation during growth of dilute $Ti_{0.92}Ta_{0.08}N$ alloys in a hybrid Ta-HIPIMS/Ti-DCMS mode, using a substrate bias applied synchronously with the metal–ion rich portions of the HIPIMS pulses, eliminates both inter- and intracolumn porosity due to effective near-surface atomic mixing allowing us to obtain essentially fully dense polycrystalline films. As a result, film hardness and elastic modulus increase dramatically. For $Ti_{0.92}Ta_{0.08}N$ films grown with $V_s = 160$ V, $H = 25.9$ GPa, and $E = 497$ GPa, while the residual film stress remains low, $\sigma = -0.7$ GPa, due to the short HIPIMS duty cycle (2%). Film surfaces are smoother [see Figs. 3(b), 3(c), and 4] and pointed conical column tops are flattened. Further increases in V_s do not significantly enhance H and E, but slowly increase the residual compressive stress.

The effect of dilute alloying is minor compared to microstructure modification via heavy-metal ion irradiation. This is clearly demonstrated by comparing the film hardness and elastic modulus results for DCMS TiN and $Ti_{0.92}Ta_{0.08}N$ layers grown with no applied heating ($T_s < 120$ °C), $V_s = 10$ V, and no Ta ion bombardment (target material ionization during DCMS sputtering is negligible). H increases from 7.8 for DCMS TiN ($T_s < 120$ °C) to 9.8 GPa for DCMS

$Ti_{0.92}Ta_{0.08}N$ ($T_s < 120$ °C), while E increases from 248 to 286 GPa as a result of dilute alloy formation. These increases are small compared to the effects of Ta^+ ion irradiation. Ta-HIPIMS/Ti-DCMS $Ti_{0.92}Ta_{0.08}N$ layers grown under synchronized substrate bias $V_s = 160$ V exhibit $H = 25.9$ GPa and $E = 497$ GPa, while the residual stress remains low (-0.7 GPa).

$Ti_{1-x}Ta_xN$ hardness can also be increased by raising the TaN alloy concentration through increases in the peak HIPIMS current density J_T for the same pulse width (corresponding to higher pulse energies E_p). However, this comes at the expense of increasing compressive stress.

Pulsed Ti^+/Ti^{2+} metal-ion irradiation during Ti-HIPIMS/Ti-DCMS is not as effective as higher-mass Ta^+/Ta^{2+} bombardment in densifying the growing film. Hence, Ti-HIPIMS/Ti-DCMS TiN layers have much lower hardnesses (e.g., $H = 13.8$ GPa with $V_s = 160$ V) than Ta-HIPIMS/Ti-DCMS $Ti_{0.92}Ta_{0.08}N$ layers ($H = 25.9$ GPa) grown with the same V_s. A crude first estimate of the maximum energy deposited to primary recoils by the incoming ion can be obtained by assuming 180° hard-sphere collisions of 160 eV Ta^+ ions ($m_{Ta} = 180.95$ amu) with $Ti_{0.92}Ta_{0.08}N$ (average film mass $m_f = 36.26$ amu) and Ti^+ ($m_{Ti} = 47.87$ amu) with TiN ($m_f = 30.94$ amu). Under these conditions, the maximum fraction of incident Ta^+ ion energy deposited into the film is $f_{Ta} = 4m_{Ta}m_f/(m_{Ta} + m_f)^2 = 0.56$ and the corresponding value for Ti^+ is $f_{Ti} = 0.95$. Thus, lower-mass Ti^+ bombardment creates higher-energy primary recoils (maximum recoil energy $E_{r,max} = 152$ eV). A larger number of recoils with lower energy ($E_{r,max} = 90$ eV) are produced with Ta^+ bombardment. This difference becomes even more pronounced for doubly charged metal ions, which constitute a significant fraction of the metal–ion flux incident at the growth surface (see Fig. 1), $E_{r,max} = 304$ eV for Ti^{2+} versus 180 eV for Ta^{2+}.

A better estimate of energy deposition effects during film growth is obtained based upon Monte Carlo TRIM[36] simulations. We characterize displacement cascades for heavier Ta ions versus lighter Ti ions, including ion ranges, depth profiles, and energy distributions of primary recoils, for 160 eV Ti bombardment of TiN and Ta bombardment of

TABLE I. TRIM simulation results for 160 eV Ti irradiation of TiN and Ta irradiation of $Ti_{0.92}Ta_{0.08}N$. $E_{r,i}$ are the average primary recoil energies and $\xi_{r,i}$ values are the effective recoil depths for $i =$ N, Ti, and Ta.

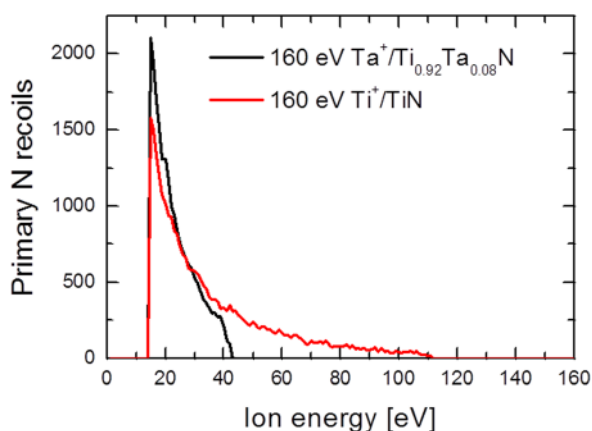|	160 eV Ti	160 eV Ta
N primary recoils/ion	1.4	1.1
Ti primary recoils/ion	1.8	2.0
Ta primary recoils/ion	–	0.2
$\langle E \rangle_{r,N}$ (eV)	36	24
$\langle E \rangle_{r,Ti}$ (eV)	45	40
$\langle E \rangle_{r,Ta}$ (eV)	–	52
$\xi_{r,N}$ (Å)	12	13
$\xi_{r,Ti}$ (Å)	13	16
$\xi_{r,Ta}$ (Å)	–	19
ξ_{r,Ti^+} (Å)	14	–
ξ_{r,Ta^+} (Å)	–	25

FIG. 9. (Color online) Energy distributions, obtained from TRIM simulations, of primary N recoils due to 160 eV Ta irradiation of $Ti_{0.92}Ta_{0.08}N$ and 160 eV Ti irradiation of TiN.

$Ti_{0.92}Ta_{0.08}N$ (see Table I). While TRIM is not accurate enough at low ion energies for quantitative evaluation, it does provide useful qualitative insights. Ta^+ creates ∼20% more primary cation recoils per incident ion, 2.0 Ti and 0.2 Ta versus 1.8 Ti recoils per ion for Ti^+, and ∼20% fewer N recoils per ion, 1.1 versus 1.4.

Due to the large mass mismatch between Ta^+ and N, only 22% of the incident ion energy is deposited into N primary recoils, while for Ti^+ bombardment the fraction is 39%, almost twice as large. Moreover, there are important differences in the energy distribution of the primary recoils for both cases, see Figs. 9 and 10. For Ta^+ irradiation, the N primary recoil energy $E_{r,N}^{Ta^+}$ is ≤42 eV, while for Ti^+, there is a high energy $E_{r,N}^{Ti^+}$ tail extending to 110 eV. Similarly, a high-energy component is present for Ti primary recoils under Ti^+ bombardment, $E_{r,Ti}^{Ti^+}$ extends to 160 eV because of the perfect mass match between ion and target atom. For Ta^+ ions, the maximum energy of Ti recoils $E_{r,Ti}^{Ta^+} = 106$ eV, and there are a larger number of Ti recoils with energy 20–60 eV. Thus, TRIM results indicate an increased number of Ti primary recoils with lower recoil energies for Ta^+/Ta^{2+} versus Ti^+/Ti^{2+} ions.
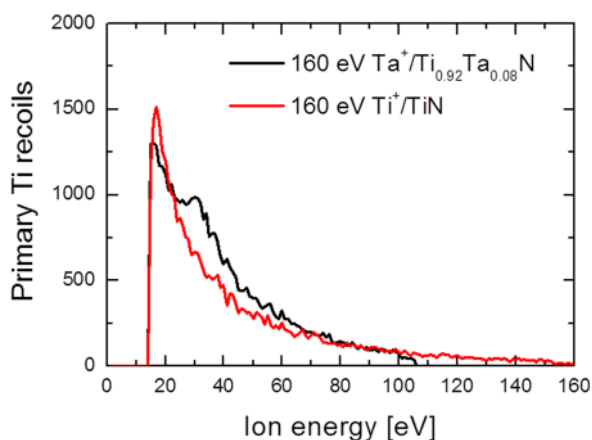

FIG. 10. (Color online) Energy distributions, obtained from TRIM simulations, of primary Ti recoils due to 160 eV Ta irradiation of $Ti_{0.92}Ta_{0.08}N$ and 160 eV Ti irradiation of TiN.

In addition, Ta^+ collision cascades extend over larger depths than these of Ti^+. The cascade for a given species is characterized by an effective depth ξ_r, the sum of the projected range r_p and straggle Δr_p.[56] Results for Ta^+ and Ti^+ primary ions as well as Ti, Ta, and N recoils are given in Table I. The cascade generated by 160 eV Ti^+ ions has a depth of ∼13 Å for all three species: Ti primary ions and Ti and N recoils. With Ta^+ bombardment, N recoils also extend to ∼13 Å, while the cation species, Ti and Ta, have longer ranges of 16 and 19 Å, respectively. The primary Ta^+ ions, because of their high mass, scatter at much smaller angles than Ti^+ and thus penetrate deeper, to 25 Å. Thus, both the primary Ta^+ metal ions and the recoiled Ta lattice atoms penetrate deeper into the near-surface region to dynamically fill residual vacancies, which result from very-low-temperature growth ($T_s/T_m < 0.12$). Ta-HIPIMS with synchronous metal–ion bias is much more effective in film densification than Ti-HIPIMS, as shown by XTEM (Fig. 3) and XRR results, giving rise to higher hardness and elastic modulus values with—depending on the choice of HIPIMS duty cycle, ion flux, ion charge, and substrate bias—low residual film stress.

In order to achieve densification, two conditions have to be satisfied simultaneously: (1) the ion dose and (2) the ion penetration range ξ_{ion} have to be sufficiently high that the extent of the near-surface intermixing zone, defined by the average effective depth of collision cascades, ξ_{mix} ∼ 10–30 Å (depending on the mass and energy of the collision partners), is larger than the DCMS layer thickness deposited between successive HIPIMS pulses. Moreover, the number of recoils created per metal atom deposited between the pulses has to be sufficiently high to ensure adequate adatom displacements in the newly deposited DCMS layer to achieve full densification. In the present $Ti_{0.92}Ta_{0.08}N$ experiments, the TiN thickness deposited between pulses h_{TiN} is 0.022 ML, while the TiN and the TaN thicknesses deposited during a HIPIMS pulse are 0.00045 and 0.002 ML, respectively. Thus, the real-time TaN deposition rate is 9× higher than that of TiN; however, the time-averaged rate is 11× lower. Dynamic near-surface mixing due to Ta^+/Ta^{2+} ion irradiation during HIPIMS pulses is very effective for two reasons: (1) $\xi_{mix} \gg h_{TiN}$, and (2) the high real-time TaN deposition rate leads to strongly overlapping collision cascades.

With $x = 0.08$, metal–ion-synchronized $V_s = 160$ V, a duty cycle of 2%, $T_s \leq 120$ °C, and $h_{TiN} = 0.022$ ML, residual stresses in $Ti_{0.92}Ta_{0.08}N$ films are low. This is predominantly due to the fact that irradiation by gas ions is suppressed due to the synchronous biasing.[21] Moreover, the metal bombarding ions are film constituents and primarily incorporated into lattice sites, consistent with the increased relaxed lattice parameter [see Fig. 2(b) and Sec. III C], resulting in relatively low residual defect concentrations. The above benefits of pulsed heavy-ion irradiation during very low-temperature film growth cannot be achieved by bombardment with heavy gas ions such as Xe^+ ($m_{Xe} = 131.29$ amu) since a sufficient flux to cause densification will also result in a high compressive stress.[57]

Further increase in the incident Ta^+/Ta^{2+} flux, hence the TaN film concentration x, while maintaining the TiN growth

rate constant, is not a preferred strategy for increasing film density, H, and E, as it leads to higher residual stress values (see Sec. III E).

The densification mechanism demonstrated here is not limited to the addition of Ta ions. Other group-VI transition metals with sufficiently high mass and low ionization potential, comparable to that of Ta ($m = 180.95$ amu and $IP_1 = 7.91$ eV), to ensure significant ionization during HIPIMS pulses, such as Hf ($m = 178.49$ amu and $IP_1 = 6.85$ eV) or W ($m = 183.84$ amu, $IP_1 = 8.01$ eV), would provide the same benefits. In addition, the pulsed heavy-metal–ion irradiation process demonstrated here can also be applied to multicathode systems in which several targets operate in DCMS mode to provide high deposition rates, while heavy-metal–ion bombardment is supplied from one or more HIPIMS sources.

V. CONCLUSIONS

We demonstrate a new process to obtain fully dense refractory ceramic thin films with high hardness and elastic modulus, and low residual stress, at T_s near room temperature ($T_s/T_m < 0.12$). The procedure is based upon reactive hybrid HIPIMS/DCMS co-sputtering in which the substrate bias is applied synchronously with the metal–ion-rich portions of the HIPIMS pulses. The primary target, Ti in the present example, operates in DCMS mode providing a continuous flux of sputter-ejected metal atoms to sustain a high deposition rate, while a high-mass/low-IP_1 target metal, Ta, is driven by HIPIMS to serve as a pulsed source of energetic metal–ions to irradiate the growth surface and densify dilute $Ti_{1-x}Ta_xN$ alloy layers. No external heating is used. As a result of heavy-metal–ion bombardment, the inter- and intracolumnar porosity, typical of low-deposition-temperature refractory ceramic thin film growth, is eliminated due to effective near-surface atomic mixing, as evidenced by XTEM, XSEM, and XRR results. The upper limit for the DCMS layer thickness grown between successive HIPIMS pulses is set by the depth of the near-surface mixing zone ξ_{mix}, which is controlled by the choice of the film elemental masses and the metal–ion energy.

For the model $Ti_{0.92}Ta_{0.08}N$ alloy films, grown by Ta-HIPIMS/Ti-DCMS at $T_s \leq 120\,°C$ with the bias voltage $V_s = 160$ V synchronized to the Ta^+/Ta^{2+} portions of the HIPIMS pulses, discussed in this article, film hardness and elastic modulus are 330 and 200% higher than corresponding values for reference DCMS TiN ($V_s = 10$ V) layers, while the residual stress remains low. The effect of dilute alloying on enhanced mechanical properties of Ta-HIPIMS/Ti-DCMS $Ti_{0.92}Ta_{0.08}N$, relative to DCMS TiN, films is small as compared to the effect of microstructure densification caused by heavy-metal Ta^+/Ta^{2+} ion irradiation. Pulsed Ti^+/Ti^{2+} metal–ion irradiation during Ti-HIPIMS/Ti-DCMS is not nearly as effective as higher-mass Ta^+/Ta^{2+} bombardment in densifying the growing film. This is interpreted with the help of TRIM simulations, which show an increased number of Ti lattice-atom primary recoils with lower recoil energies, and deeper collision cascades, for Ta^+/Ta^{2+} versus

Ti^+/Ti^{2+} ions. Additional lattice relaxation is provided by the high real-time ion flux, during the pulses, resulting in strongly overlapping collision cascades.

Residual defect concentrations are low under Ta^{n+} bombardment, since Ta is primarily incorporated into the lattice of the growing alloy film, giving rise to an increased relaxed lattice parameter, resulting in low residual stress values. These results are not possible to achieve by bombardment with heavy noble-gas ions such as Xe^+ ($m_{Xe} = 131.29$ amu), of similar energy, which become incorporated as interstitials.

High hardness and low residual stress obtained for Ta-HIPIMS/Ti-DCMS $Ti_{0.92}Ta_{0.08}N$ alloys grown at $T_s \leq 120\,°C$ indicate that the heavy-metal ion momentum transfer to the growing film provides sufficient adatom mobility and near-surface intermixing at T_s near RT to substitute for the thermally driven adatom diffusion even at $T_s = 500\,°C$.

APPENDIX: TEMPERATURE RISE DURING FILM GROWTH

Figure 11 shows substrate temperatures T_s as a function of time t during film growth, with no externally applied substrate heating, of Ta-HIPIMS/Ti-DCMS $Ti_{1-x}Ta_xN$ alloys deposited using a metal–ion-synchronized pulsed bias $V_s = 160$ V, and DCMS TiN films with $V_s = V_f = 10$ V. $Ti_{1-x}Ta_xN$ results are shown for three different TaN concentrations: $x = 0.08$ ($E_p = 5$ J, $J_T = 0.21$ A/cm^2), $x = 0.13$ ($E_p = 10$ J, $J_T = 0.53$ A/cm^2), and $x = 0.16$ ($E_p = 15$ J, $J_T = 0.93$ A/cm^2. The starting temperature in all cases, following thermal degassing of the Si(001) substrates prior to film deposition, is $T_s = 65 \pm 1\,°C$.
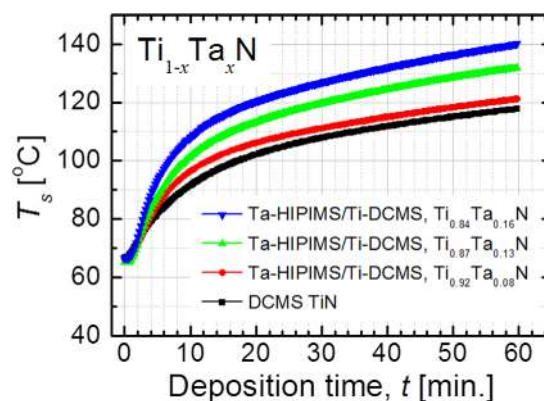

FIG. 11. (Color online) Substrate temperatures T_s as a function of deposition time t during growth of Ta-HIPIMS/Ti-DCMS $Ti_{1-x}Ta_xN$ ($x = 0.08$, 0.13, and 0.16) with $V_s = 160$ V synchronized to the metal–ion-rich portions of HIPIMS pulses, and DCMS TiN films grown with $V_s = 10$ V. In all cases, there is no external heating of the Si(001) substrates.

All $T_s(t)$ curves are composed of two distinct regions. $T_s(t)$ increases rapidly during the first ~10 min with a heating rate dT_s/dt of ~2.6 °C/min for TiN and 3.1 °C/min for $Ti_{0.92}Ta_{0.08}N$ deposition. The initial heating rate dT_s/dt increases to 3.7 and 4.3 °C/min for $Ti_{1-x}Ta_xN$ alloys with $x = 0.13$ and 0.16. In all cases, dT_s/dt decreases at longer deposition times and becomes nearly constant for the final 30 min at 0.32 °C/min for TiN and 0.33 °C/min for $Ti_{0.92}Ta_{0.08}N$, increasing to 0.4 °C/min for alloys with $x = 0.13$ and 0.43 °C/min with $x = 0.16$. For the reference DCMS TiN film, T_s reaches 118 °C during 60 min deposition runs, while for $Ti_{0.92}Ta_{0.08}N$, T_s reaches 120 °C.

[1]D. M. Mattox and G. J. Kominiak, J. Vac. Sci. Technol. **9**, 528 (1972).

[2]G. Hakansson, J.-E. Sundgren, D. McIntyre, J. E. Greene, and W.-D. Munz, Thin Solid Films **153**, 55 (1987).

[3]I. Petrov, P. B. Barna, L. Hultman, and J. E. Greene, J. Vac. Sci. Technol. A **21**, S117 (2003).

[4]L. Hultman, J.-E. Sundgren, J. E. Greene, D. B. Bergstrom, and I. Petrov, J. Appl. Phys. **78**, 5395 (1995).

[5]F. Adibi, I. Petrov, J. E. Greene, L. Hultman, and J.-E. Sundgren, J. Appl. Phys. **73**, 8580 (1993).

[6]T. C. Huang, G. Lim, F. Parmigiani, and E. Kay, J. Vac. Sci. Technol. A **3**, 2161 (1985).

[7]J. E. Greene, *Deposition Technologies for Films and Coatings*, edited by R. F. Bunshah (Noyes, Park Ridge, NJ, 1994), p. 681.

[8]A. Anders, *Cathodic Arcs*, Springer Series on Atomic, Optical, and Plasma Physics Vol. 50 (Springer Science+Business Media, LLC, New York, 2009).

[9]V. Kouznetsov, K. Macak, J. M. Schneider, U. Helmersson, and I. Petrov, Surf. Coat. Technol. **122**, 290 (1999).

[10]T. Lee, H. Seo, H. Hwang, B. Howe, S. Kodambaka, J. E. Greene, and I. Petrov, Thin Solid Films **518**, 5169 (2010).

[11]J. E. Greene, "Thin Film Nucleation, Growth: Microstructural Evolution: An Atomic Scale View," in *Handbook of Deposition Technologies for Thin Films and Coatings*, 3rd ed., edited by P. Martin (William Andrew, Burlington, MA, 2010).

[12]H. Oettel, R. Wiedemann, and S. Preisler, Surf. Coat. Technol. **74–75**, 273 (1995).

[13]C. V. Falub, A. Karimi, M. Ante, and W. Kalss, Surf. Coat. Technol. **201**, 5891 (2007).

[14]A. Hörling, L. Hultman, M. Odén, J. Sjölén, and L. Karlsson, J. Vac. Sci. Technol. A **20**, 1815 (2002).

[15]J. A. Thornton, J. Vac. Sci. Technol. A **4**, 3059 (1986).

[16]J. M. E. Harper, J. J. Cuomo, and R. J. Gambino, *Ion Bombardment Modification of Surfaces: Fundamentals and Applications*, edited by O. Auciello and R. Kelly (Elsevier, Amsterdam, 1984).

[17]H. F. Winters and E. Kay, J. Appl. Phys. **38**, 3928 (1967).

[18]J. A. Thornton, J. Tabock, and D. W. Hoffman, Thin Solid Films **64**, 111 (1979).

[19]G. Greczynski, J. Lu, M. Johansson, J. Jensen, I. Petrov, J. E. Greene, and L. Hultman, Surf. Coat. Technol. **206**, 4202 (2012).

[20]G. Greczynski, J. Lu, M. Johansson, J. Jensen, I. Petrov, J. E. Greene, and L. Hultman, Vacuum **86**, 1036 (2012).

[21]G. Greczynski *et al.*, J. Vac. Sci. Technol. A **30**, 061504 (2012).

[22]V. Petrman and J. Houska, J Mater Sci **48**, 7642 (2013).

[23]A. M. James and M. P. Lord, *Macmillan's Chemical and Physical Data* (Macmillan, London, UK, 1992).

[24]J. E. Huheey, E. A. Keiter, and R. L. Keiter, *Inorganic Chemistry: Principles of Structure and Reactivity*, 4th ed. (HarperCollins, New York, USA, 1993).

[25]*CRC Handbook of Chemistry and Physics*, 84th ed., edited by David R. Lide, Section 10, Atomic, Molecular, and Optical Physics; Ionization Potentials of Atoms and Atomic Ions (CRC, Boca Raton, FL, 2003).

[26]See: http://www.cemecon.de/coating_technology/coating_units/hipims_sputter_coating_system/index_eng.html, accessed in June 2014.

[27]Thermocouple calibrations are confirmed using boiling water; the maximum allowable deviation is ±0.2 °C.

[28]Current densities reported here are determined based upon the full flat-target area. Current densities based upon the shape of the erosion pattern following the experiments are estimated as 0.31 A/cm² with $E_p = 5$ J, 0.82 A/cm² with $E_p = 10$ J, and 1.49 A/cm² with $E_p = 15$ J.

[29]G. Greczynski and L. Hultman, Vacuum **84**, 1159 (2010).

[30]M. Mayer, AIP Conf. Proc. **475**, 541 (1999).

[31]M. Birkholz, in *Thin Film Analysis by X-ray Scattering* (Wiley-VCH, Weinheim 2006), Chap. 6.

[32]J. O. Kim, J. D. Achenbach, P. B. Mirkarimi, M. Shinn, and S. A. Barnett, J. Appl. Phys. **72**, 1805 (1992).

[33]P. Djemia, M. Benhamida, Kh. Bouamama, L. Belliard, D. Faurie, and G. Abadias, Surf. Coat. Technol. **215**, 199 (2013).

[34]W. C. Oliver and G. M. Pharr, J. Mater. Res. **7**, 1564 (1992).

[35]J. F. Ziegler, J. P. Biersack, and U. Littmark, "The stopping and range of ions in solids," in *Stopping and Ranges of Ions in Matter* (Pergamon, New York, 1984), Vol. 1.

[36]See: www.srim.org; accessed on 28 June 2013.

[37]The JCPDS database (1998), data set number: 38-1420; W. Wong-Ng, H. McMurdie, B. Paretzkin, C. Hubbard, and A. Dragoo, Powder Diffr. **2**, 191 (1987).

[38]C.-S. Shin, D.Gall, Y.-W. Kim, P. Desjardins, I. Petrov, J. E. Greene, M. Oden, and L. Hultman, J. Appl. Phys. **90**, 2879 (2001).

[39]G. Ehrlich and F. G. Hudda, J. Chem. Phys. **44**, 1039 (1966).

[40]G. Ehrlich, Surf. Sci. **331–333**, 865 (1995).

[41]G. K. Wehner and D. Rosenberg, J. Appl. Phys. **31**, 177 (1960).

[42]P. Sigmund, Phys. Rev. **184**, 383 (1969).

[43]P. Sigmund, Phys. Rev. **187**, 768 (1969).

[44]T. Ono, T. Keamotsu, and T. Muramoto, *Reactive Sputter Deposition*, edited by D. Depla and S. Mahieu (Springer, Berlin, Germany, 2008).

[45]A. M. Myers, J. R. Doyle, and D. N. Ruzic, J. Appl. Phys. **72**, 3064 (1992).

[46]L. Hultman, U. Helmersson, S. A. Barnett, J.-E. Sundgren, and J. E. Greene, J. Appl. Phys. **61**, 552 (1987).

[47]H. Ljungcrantz, M. Oden, L. Hultman, J. E. Greene, and J.-E. Sundgren, J. Appl. Phys. **80**, 6725 (1996).

[48]C.-S. Shin, D. Gall, N. Hellgren, J. Patscheider, I. Petrov, and J. E. Greene, J. Appl. Phys. **93**, 6025 (2003).

[49]M. Ohring, *Materials Science of Thin Films*, 2nd ed. (Academic, New York, 2001), pp. 732–733.

[50]H. Watanabe, N. Yamada, and M. Okaji, Int. J. Thermophys. **25**, 221 (2004).

[51]Hugh O. Pierson, *Handbook of Refractory Carbides and Nitrides: Properties, Characteristics, Processing, and Applications* (William Andrew, Burlington, MA, 1996). p. 193.

[52]N.-E. Lee, D. G. Cahill, and J. E. Greene, J. Appl. Phys. **80**, 2199 (1996).

[53]J. Krug, P. Politi, and T. Michely, Phys. Rev. B **61**, 14037 (2000).

[54]B. W. Karr, I. Petrov, D. G. Cahill, and J. E. Greene, Appl. Phys. Lett. **70**, 1703 (1997).

[55]C. Roland and H. Guo, Phys. Rev. Lett. **66**, 2104 (1991).

[56]E. F. Krimmel and H. Pfleiderer, Radiat. Effects **19**, 83 (1973).

[57]L. Hultman, C. Engstrom, J. Birch, M. P. Johansson, M. Oden, L. Karlsson, and H. Ljungcrantz, Zeitschrift Metallkunde **90**, 803 (1999).